RESEARCH ARTICLE
Rising Stars
ADVANCED MATERIALS
www.advmat.de

Selective Induction of Molecular Assembly to Tissue-Level Anisotropy on Peptide-Based Optoelectronic Cardiac Biointerfaces

*Ze-Fan Yao, Yuyao Kuang, Hao-Tian Wu, Emil Lundqvist, Xin Fu, Natalie Celt, Jian Pei, Albert F. Yee, and Herdeline Ann M. Ardoña**

The conduction efficiency of ions in excitable tissues and of charged species in organic conjugated materials both benefit from having ordered domains and anisotropic pathways. In this study, a photocurrent-generating cardiac biointerface is presented, particularly for investigating the sensitivity of cardiomyocytes to geometrically comply to biomacromolecular cues differentially assembled on a conductive nanogrooved substrate. Through a polymeric surface-templated approach, photoconductive substrates with symmetric peptide-quaterthiophene (4T)-peptide units assembled as 1D nanostructures on nanoimprinted polyalkylthiophene (P3HT) surface are developed. The 4T-based peptides studied here can form 1D nanostructures on prepatterned polyalkylthiophene substrates, as directed by hydrogen bonding, aromatic interactions between 4T and P3HT, and physical confinement on the nanogrooves. It is observed that smaller 4T-peptide units that can achieve a higher degree of assembly order within the polymeric templates serve as a more efficient driver of cardiac cytoskeletal anisotropy than merely presenting aligned -RGD bioadhesive epitopes on a nanotopographic surface. These results unravel some insights on how cardiomyocytes perceive submicrometer dimensionality, local molecular order, and characteristics of surface cues in their immediate environment. Overall, the work offers a cardiac patterning platform that presents the possibility of a gene modification-free cardiac photostimulation approach while controlling the conduction directionality of the biotic and abiotic components.

1. Introduction

The complex organization of cardiac tissues plays a key role in ensuring coordinated electrophysiological functions and efficient muscle contractions, which are critical to the ability of the heart to pump blood effectively. In the human myocardium, the precise alignment of cardiomyocytes is important for achieving normal contraction-relaxation cycling. Similar to other tissues with directionality, it is known that extracellular matrix (ECM) proteins provide topological and biochemical cues, guiding the spatially aligned arrangement and synchronous contraction of cardiomyocytes.[1–5] The dynamic interplay between the cardiomyocytes and their ECM is particularly important for the development and sustenance of proper function for cardiac tissues.[6–8] Efforts have been made to develop novel biomaterials and 3D scaffolds that mimic the properties and microenvironments of the native cardiac ECM, providing the necessary topological and biochemical cues to guide cell arrangement.[9–13] However, there remains a limited understanding as

Z.-F. Yao, Y. Kuang, A. F. Yee, H. A. M. Ardoña
Department of Chemical and Biomolecular Engineering
Samueli School of Engineering
University of California
Irvine, CA 92697, USA
E-mail: hardona@uci.edu
Z.-F. Yao, H. A. M. Ardoña
Department of Chemistry
School of Physical Sciences
University of California
Irvine, CA 92697, USA
The ORCID identification number(s) for the author(s) of this article can be found under https://doi.org/10.1002/adma.202312231

DOI: 10.1002/adma.202312231

H.-T. Wu, J. Pei
Beijing National Laboratory for Molecular Sciences (BNLMS)
Key Laboratory of Polymer Chemistry and Physics of Ministry of Education
Center of Soft Matter Science and Engineering
College of Chemistry and Molecular Engineering
Peking University
Beijing 100871, China
E. Lundqvist, N. Celt, H. A. M. Ardoña
Department of Biomedical Engineering
Samueli School of Engineering
University of California
Irvine, CA 92697, USA
X. Fu
Department of Materials Science and Engineering
Samueli School of Engineering
University of California
Irvine, CA 92697, USA

to how cardiomyocytes perceive biophysical cues, such as the resolution of feature dimensions reflected on the ECM topography that are necessary to guide cellular organization.[8] Considering the dynamic nature of ECM microenvironments, utilizing materials that show adaptability, such as supramolecular biomaterials, has been recently considered desirable for tissue engineering applications.[14–17] The noncovalent molecular interactions for supramolecular biomaterials also assist with tunability of mechanical properties and capability to present surface cues in a dynamic manner.

In addition to the defined matrix and cellular orientation in native cardiac tissues, the excitable nature of cardiomyocytes also favors the use of conductive synthetic scaffolds for in vitro modeling applications.[18–20] Constructing in vitro conductive environments provides efficient electrical communication among these excitable cardiomyocytes, ensuring coordinated electromechanical function as manifested in their contractility.[21–23] Previous literature has reported that electrical stimulation in conductive bioscaffolds can support cardiac cell viability, help promote maturation, and facilitate and increase gap junction protein expression.[24–26] Many of the biomaterials used in field stimulation showed low spatiotemporal resolutions for cellular stimulation, which could limit the extent of mechanistic studies involving cardiac electrical signaling. As such, light-based approaches that could increase the resolution of stimulation, most of them being based on synthetic materials if not relying on optogenetics, offer a minimally invasive way of doing so.[27–29] Here, we explore the bioelectronic utility of optoelectronic π-conjugated peptides that combine the advantages of both naturally inspired biomolecules and photoexcitable moieties within a self-assembling material.[30–33] The functional π-conjugated units enable unique photophysical properties and charge transport, while the peptide moieties offer control over molecular interactions and order through sequence variation.[33–37] The supramolecular organization of these π-conjugated peptides, which has been well studied under aqueous environments, can create favorable charge transport pathways and more controllable exciton delocalization, improving their optoelectronic performance as compared to traditional π-conjugated systems. Thus, π-conjugated peptides hold significant promise for diverse applications in bioelectronics.[21,38,39] Moreover, the hierarchical assembly of π-conjugated peptides can lead to well-organized nanostructures with unique functionalities that can complement the structural requirements of artificial matrices that can regulate excitable cell morphology and behavior, such as inducing cell alignment via 1D nanostructures.[40–42] Therefore, seeking methods that allow for surface patterning of these molecularly ordered optoelectronic peptides in bioelectronic devices will truly bring out the potential of such supramolecular materials toward cardiac tissue engineering applications.[16,43–45]

In this work, we develop an optoelectronic cardiac biointerface that can facilitate surface-templated self-assembly phenomena, along with selectively inducing the molecular order of π-conjugated peptides and cardiac tissue-level anisotropy. Specifically, we create 1D nanostructures of photoconductive π-conjugated peptides on polymeric substrates for triggering the alignment of cardiomyocytes—focusing on elucidating the impacts of the ordering of biomolecular nanoassemblies here to organization in the cell and tissue monolayer level. (**Figure 1**). The π-conjugated peptides designed for this study comprise a quaterthiophene central unit and two short peptide sequences at both ends, leading to stronger intermolecular interactions of directional π–π stacking and hydrogen bonds, and allowing these peptides to form 1D nanostructures assembled in solution. On the other hand, the central π-conjugated quaterthiophenes can provide photocurrent-generating properties and capability for charge transport. The ionizable peptide sequences can interact with the aqueous environment and enable ion transport. These π-conjugated peptides share analogous conjugated structures with the presented polyalkylthiophene in the substrate materials, promoting the formation of assembled nanostructures on the polyalkylthiophene substrates. Furthermore, by utilizing nanogrooved polyalkylthiophene substrates, we can effectively achieve anisotropic 1D nanostructures of π-conjugated peptides on the surface, thereby forming aligned micrometer-long 1D nanostructures. The formation of these anisotropic nanostructures are corroborated by the assembly lengths monitored using atomic force microscopy (AFM). Consequently, these anisotropic nanostructures of π-conjugated peptides can function as nanotopographical cues that effectively induce cardiomyocyte alignment and promote the formation of anisotropic tissues through the interaction between the peptides and cardiomyocytes. Our findings support that the anisotropic self-assembly approach of supramolecular biomaterials, tailored for controlled cardiomyocyte alignment, could play a pivotal role in advancing our understanding of biointerfacing with excitable cells and facilitating the development of in vitro cardiac models. Importantly, the observation of selectivity in the induction of cardiac anisotropy reveals some insights on the ability of cardiomyocytes to perceive surface and topographical cues that are below the typical submicrometer dimensions of ECM fibers and patterns for cardiac tissues previously reported in the literature.

2. Results and Discussion

This study is centered on the development of an optoelectronic cardiac biointerface, whereby the nature and degree of order of biomolecules at the surface dictate whether cardiomyocytes interfaced with the material system can form anisotropic tissues (Figure 1). To form 1D assembly nanostructures, we designed π-conjugated peptides with a known p-type organic semiconductor quaterthiophene (4T) and short peptide sequences on each end. The peptide sequences used here are: i) triaspartic acid (DDD) as an ionizable base sequence or ii) an RGD-linked sequence (DGRDDD, C→N termini). The RGD (N→C termini) epitope is a known integrin-binding segment of fibronectin (FN), an ECM protein, which is widely used to improve cell adhesion and induce cell pattern.[46,47] These two quaterthiophene-functionalized peptides were synthesized according to the reported procedures using on-resin coupling (Figures S1,S2,S3,S4, see more details in the Supporting Information).[48,49] The central conjugated unit, 4T, and peptide termini together are capable of not only

H. A. M. Ardoña
Sue & Bill Gross Stem Cell Research Center
University of California
Irvine, CA 92697, USA

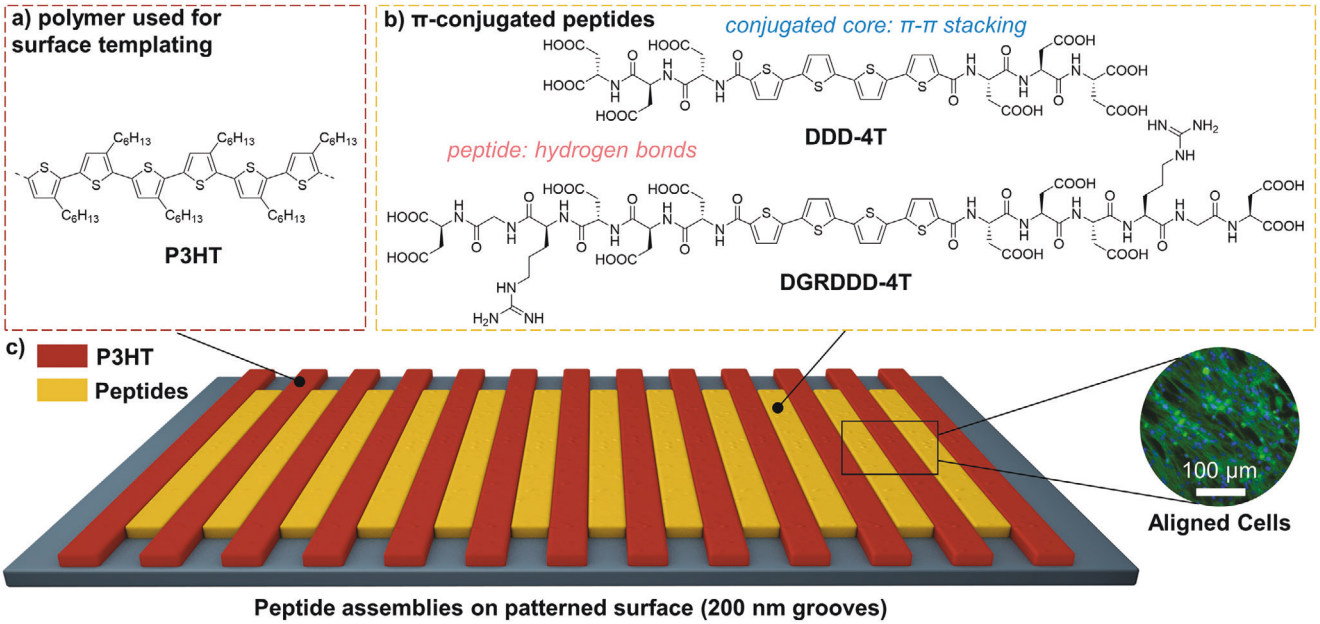

Figure 1. Induction of molecular assembly order to tissue-level anisotropic organization using nanotopographic patterns on optoelectronic cardiac biointerfaces. a) Chemical structure of the semiconducting polymer used to create imprinted substrates: poly(3-hexylthiophene) (P3HT). b) Chemical structures of optoelectronic π-conjugated peptides, DDD-4T and DGRDDD-4T. c) Idealized schematic illustration of the nanopatterned surface-templated assembly of π-conjugated peptides and its effect on cardiomyocyte tissue alignment.

assembling into 1D nanostructures through π-interactions and hydrogen bonds, but also of facilitating electronic and ionic charge transport.[49,50] On the other hand, a widely used conjugated polymer, poly(3-hexylthiophene) (P3HT), was adopted as the substrate template material due to the similar conjugated backbone with the quaterthiophene core of the peptide units. The π-interactions between quaterthiophene and polythiophene are leveraged here to facilitate peptide-surface interactions, guiding the self-assembly process on the polymeric substrate (Figure 1). P3HT films were nanoimprinted to give straight line patterns (nanogrooves) on the glass as the template for forming aligned 1D nanostructures of π-conjugated peptides (Figure S5, Supporting Information). In brief, the nanopatterned P3HT films were used as the surface template to guide the peptide assembly for 1D nanostructures.

The self-assembly process of the selected π-conjugated peptides in aqueous environments, as dictated by the peptide sequence design, can be initiated by pH changes. With three aspartic acids as the peripheral group, the assembly of the supramolecular synthons used here can be triggered under acidic conditions. We first systemically studied the pristine assembly behavior of the π-conjugated peptides in aqueous solutions, involving the observation and analysis of absorbance, photoluminescence (PL), and circular dichroism (CD) spectra. The transition from pH 6 to 2, led to the complete protonation of carboxyl groups within the peptides. Hence, the protonation minimized the electrostatic repulsive forces stemming from the negatively charged entities, thereby promoting associative intermolecular interactions. Consequently, the molecules could assemble into 1D nanostructures (pH 2) from dissolved conditions (pH 6). Upon acidification, DDD-4T and DGRDDD-4T exhibited a significant decrease in absorbance intensity and a slight blueshift in maximum peaks, reminiscent of an H-like aggregation (**Figure 2**a,b). Furthermore, it was evident that both DDD-4T and DGRDDD-4T experienced quenched PL intensity under acidic conditions. Notably, DGRDDD-4T demonstrated a larger Stokes shift when compared to DDD-4T. This differential shift implies that the excited state of DGRDDD-4T is more profoundly relaxed by the surrounding solvent environment, which could be attributed to the elongated hydrophilic peptide sequence of DGRDDD.[51] CD spectra provided direct evidence of chiral assemblies formed by quaterthiophene-based conjugated peptides in solutions, as indicated by the strong Cotton effect observed for both peptides within the range of 300–500 nm (Figure S6, Supporting Information).

In order to gain a deeper understanding of the molecular packing and interactions involved in forming 1D assemblies, molecular simulations were conducted for DDD-4T and DGRDDD-4T assemblies. Structural models were built using 20 molecules of DDD-4T or DGRDDD-4T with twisted stacked structures and further optimized based on reported structural models (Figure 2c,d; and Figure S7, Supporting Information).[49,52–54] The optimized structures clearly show the chiral nature of the stacking in DDD-4T and DGRDDD-4T, agreeing well with the CD results. Benefiting from the designed molecular structures, the central π–π stacking of quaterthiophenes is projected to enable photocurrent generation and support electron/exciton transport. Meanwhile, the hydrophilic peptide sequences can interact with the aqueous environment and support ion transport. Based on our generated structural models, DGRDDD-4T, with a longer peptide sequence length than DDD-4T, showed more hydrogen bonding sites within the peptide parts or interacted with environmental water molecules, which corresponds to the more extended aggregates as observed from microscopy analyses. The

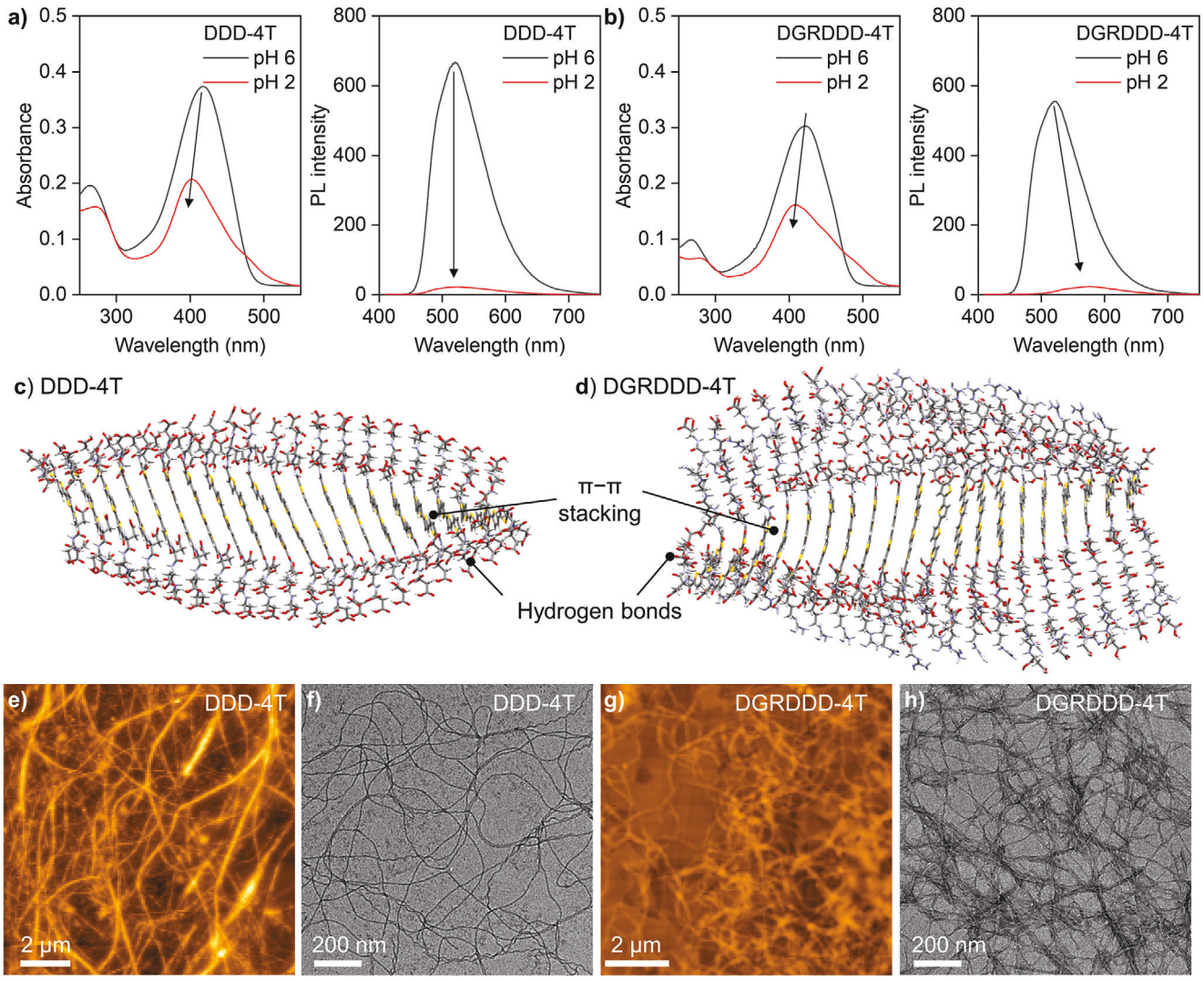

Figure 2. Self-assembly of π-conjugated peptides under aqueous environments. a,b) Absorbance and photoluminescence (PL) profiles of DDD-4T and DGRDDD-4T (pH 2 and pH 6). c,d) Optimized assembly geometries of stacked 20 molecules of DDD-4T and DGRDDD-4T. The π-stacking of quaterthiophenes and ionizable groups of peptide sequences could facilitate electron and ion transport, respectively. e,f) AFM height image and TEM images of DDD-4T (pH 2). g,h) AFM height image and TEM images of DDDDGR-4T (pH 2).

molecular simulations correlated well with the experimental characterizations for 1D nanostructure formation and provided a more detailed structural understanding of the peptide assembly and interactions at the molecular level. The assembly morphologies of DDD-4T and DGRDDD-4T formed under aqueous conditions were visualized with atomic force microscope (AFM) and transmission electron microscope (TEM), employing acidified solutions at pH 2 with a concentration of 1 mM. DDD-4T exhibited consistent 1D nanostructures as confirmed by both AFM (Figure 2e) and TEM (Figure 2f) images. Meanwhile, DGRDDD-4T showed similar 1D aggregates, albeit appearing as broader and with more bundled structures than DDD-4T (Figure 2g,h). Additionally, even 2D aggregates could be found within the same sample that predominantly exhibited 1D aggregates in AFM images (Figure S8, Supporting Information). This observation is potentially attributed to the elongated hydrophilic peptide sequence and more hydrogen bonding sites in DGRDDD-4T.

To guide the formation of 1D nanostructures of designed peptides on nanogrooved P3HT surface, P3HT films were first fabricated by spin-coating on glass substrates and then patterned using a nanoimprinting process with a premade polydimethylsiloxane (PDMS) stamp (Figure S5, Supporting Information).[55–59] The nanoimprinted P3HT showed uniform line patterns with about 200 nm in width and 80 nm in depth, enabling precise control over surface topography (Figure S9, Supporting Information). We note that the width chosen here is 100 times smaller than those typically used for in vitro patterning cardiac tissues via lithography techniques (~20 μm), and also below the threshold of micrometer-scale fibers of native matrices.[60–62] These P3HT substrates were used as templates for guiding the self-assembly process of π-conjugated peptides due to the combination of the π–π interactions and nanoconfinement effect. The nanopatterned P3HT substrates were first incubated with the peptide solution with an optimized concentration of 10 μM (Figure S10,

Supporting Information). The substrates were then taken from the solution after specific incubation times following natural drying under ambient conditions. As shown in the AFM height images, DDD-4T formed 1D nanostructures on the substrate surface, preferentially aligned along the line patterns (**Figure 3**a; and Figure S11, Supporting Information). With increasing incubation time ranging from 2, 4, 8, 24, and 72 h, the average length of 1D nanostructures significantly increased from 0.64 ± 0.05, 1.10 ± 0.11, 1.98 ± 0.18, 1.94 ± 0.17, and 2.35 ± 0.15 μm, respectively (Figure 3e,f). These results suggest that with the incubation protocol we used, it takes about ~8 h to form 1D structures with an average nanostructure length of ~2 μm. Since the RGD sequence can enhance cell adhesion, we doped the DDD-4T assembly with the bioadhesive epitope-bearing DRGDDD-4T. At 20 mol% doping of DDD-4T with DRGDDD-4T (discussed below as the ratio with the most efficient cell alignment induction across other doping mol%), similar 1D assembly structures were observed for the blend as the DDD-4T, but with more dispersed distribution and shortened aggregate length (Figure S12, Supporting Information). The disparity between the sizes of the structure might be due to the extended peptide interactions as discussed above (Figure 2; and Figure S8, Supporting Information). The assembly length distribution saturated after 8 h incubation, suggesting that the incubation would facilitate the limited nucleation sites on the substrate. Based on the control experiments conducted with other substrates, we found that using hydrophobic PDMS substrates with the same line patterns (Figure 3b) or P3HT substrates without patterns (Figure 3c) or bare SiO_2/Si substrates (Figure 3d) could not result in an apparent formation of 1D nanostructures of DDD-4T using the same protocol. Fast Fourier transforms (FFT) of these AFM height images illustrate the formation of anisotropic 1D assemblies of DDD-4T formed on patterned P3HT film as compared to other substrates used. The results from these control experiments confirm the importance of patterns and the interactions that can be facilitated between the monomer units and the substrate. We conclude that both assembly-surface interactions (enhanced π–π interactions between P3HT and DDD-4T) and physical nanoconfinement effect are necessary to guide the 1D assembly of π-conjugated peptides.

Grazing incidence wide-angle X-ray scattering (GIWAXS) was conducted on the peptides assembled on polymer films to gain insights on the degree of ordering or molecular packing of the assemblies formed on nanoimprinted substrates. Compared with the dropcasted peptides on SiO_2/Si substrate, the peptide assemblies on patterned P3HT showed similar diffraction peaks at 1.9 and 2.3 $Å^{-1}$ for DDD-4T, while blends of 20% DGRDDD-4T with 80% DDD-4T showed a weaker diffraction peak at 2.3 $Å^{-1}$ (**Figure 4**a,b) suggesting that the blending with the longer peptide sequence could be perturbing the molecular order of pristine DDD-4T. The GIWAXS patterns of the peptide assemblies on P3HT exhibited isotropic diffraction rings, suggesting the peptides formed mixed packing with coexist of edge-on and face-on modes. These diffraction results still indicate that the π-conjugated peptides of DDD-4T and DGRDDD-4T could maintain the close π-stacking structures in the 1D assemblies when confined within the nanoscale channels of P3HT substrates (Figure 4c). Intimate molecular packing would favor the electronic coupling between adjacent molecules and charge transport along the molecular assemblies.[63] Since the π-conjugated peptides have been demonstrated to facilitate photoinduced electron or energy transport,[32,36,64–66] we measured the photocurrent performance of these peptide assemblies formed on substrates with gold as electrodes (Figure 4d). After deposition of the peptide assemblies on the P3HT surface, the samples showed enhanced photocurrent compared with the pristine P3HT. Importantly, all these polymer/peptide substrates showed photocurrent generation properties under the illumination of a 415 nm LED light source (16 mW cm^{-2}, 2 Hz) (Figure 4e). Quantitatively, DDD-4T and the blend with DGRDDD-4T on P3HT exhibited photocurrent of peak values of 0.357 ± 0.004 and 0.214 ± 0.004 nA, respectively, showing significantly enhanced photocurrent compared to a P3HT thin film of 0.121 ± 0.003 nA (average values with standard error of the mean, $N = 120$ peaks from 3 devices, Figure S13, Supporting Information). Meanwhile, all the samples showed consistent frequency of the photocurrent peaks as the illumination frequency of 2 Hz, according to the photocurrent curves and corresponding FFT patterns (Figure 4e; and Figure S14, Supporting Information). These results suggest that the designed π-conjugated peptides can generate photocurrents, specifically leading to enhanced photocurrent generation compared with pristine P3HT. Hence, our polymeric surface templated assembly strategy of π-conjugated peptides could potentially lead to more efficient photostimulation performance in the future.

Finally, considering that the alignment of cardiomyocytes is essential for the proper functioning of cardiac tissues, we sought to investigate how the features presented on the photoconductive surfaces we developed here impact the organization of cardiomyocytes seeded on top of such materials.[12,67–70] In particular, we asked whether neonatal rat ventricular myocytes (NRVMs) would comply with the topographical cues provided by the following surfaces: i) bare nanoimprinted P3HT substrate; ii) nanoimprinted P3HT substrate coated with fibronectin (FN; an ECM protein, commonly used in patterning protocols and concentrations that are optimized for other 2D substrates); iii) DDD-4T assembled on nanoimprinted P3HT substrates; and iv) DGRDDD-4T and DDD-4T blend assembled on nanoimprinted P3HT substrates. Among this set, only those with the 1D nanostructures of π-conjugated peptides assembled on nanoimprinted P3HT substrates induced the alignment of cardiomyocytes, as measured based on the distribution of cell angle with respect to the material pattern, as well as through the orientational order parameter (OOP) values measured for the respective cytoskeletal and sarcomeric orientation under each substrate condition (**Figure 5**). Specifically, we first measured the cell orientation angles and corresponding distribution from the brightfield images to compare the surface topography and assembly order effect on cellular orientation. As a point of reference, seeded NRVMs showed random orientation after 5 days of incubation on patterned P3HT, both bare and FN-coated samples (Figure 5a), implying that the nanotopography alone of the P3HT substrates used here (200 nm widths) could not effectively induce the cell alignment. To note, nanopatterned or micropatterned polymeric substrates have been previously demonstrated to act as topographical cues to induce effective cell alignment for various types of cells, such as with PDMS, polyethylene glycol (PEG), or methacrylated gelatin (GelMA) films with nanogroove widths ranging from 50–250 nm to 30–40 μm.[41,71–74] For cardiac tissues in particular, the

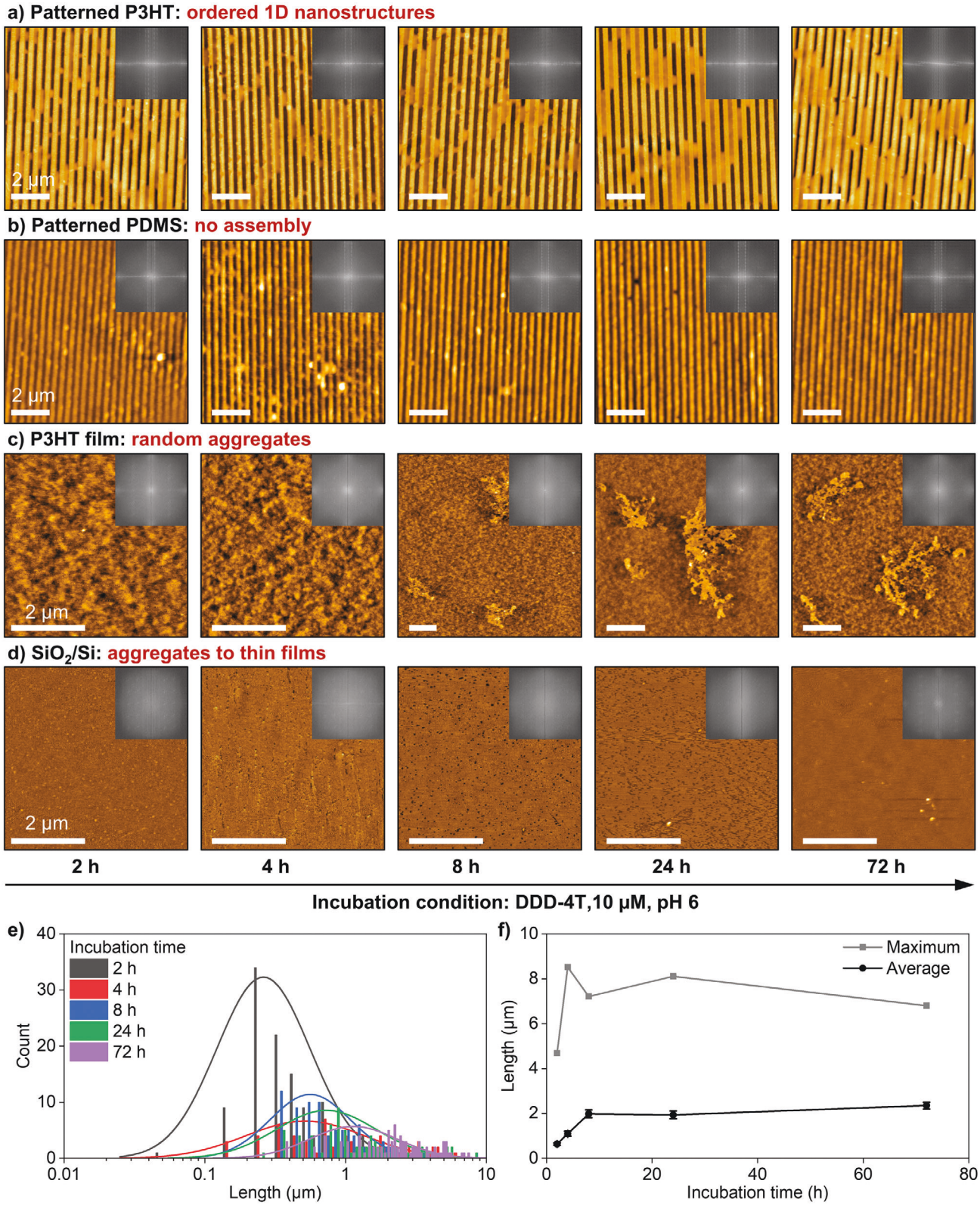

Figure 3. Kinetic evaluation of assembly growth of DDD-4T on nanopatterned P3HT surface and control surfaces. a) AFM height images of incubated samples on patterned P3HT. b) AFM height images of incubated samples on patterned PDMS. c) AFM height images of incubated samples on non-patterned P3HT film. d) AFM height images of incubated samples on SiO_2/Si. e) Length distribution of DDD-4T assembly on nanopatterned P3HT. All scale bars in (a–d) are 2 µm. Corresponding FFT patterns are provided as inset with the AFM height images. e) Length evolution of DDD-4T assembly on nanopatterned P3HT. Maximum and average values with standard error of the mean are provided from the measured length of 80–130 aggregates.

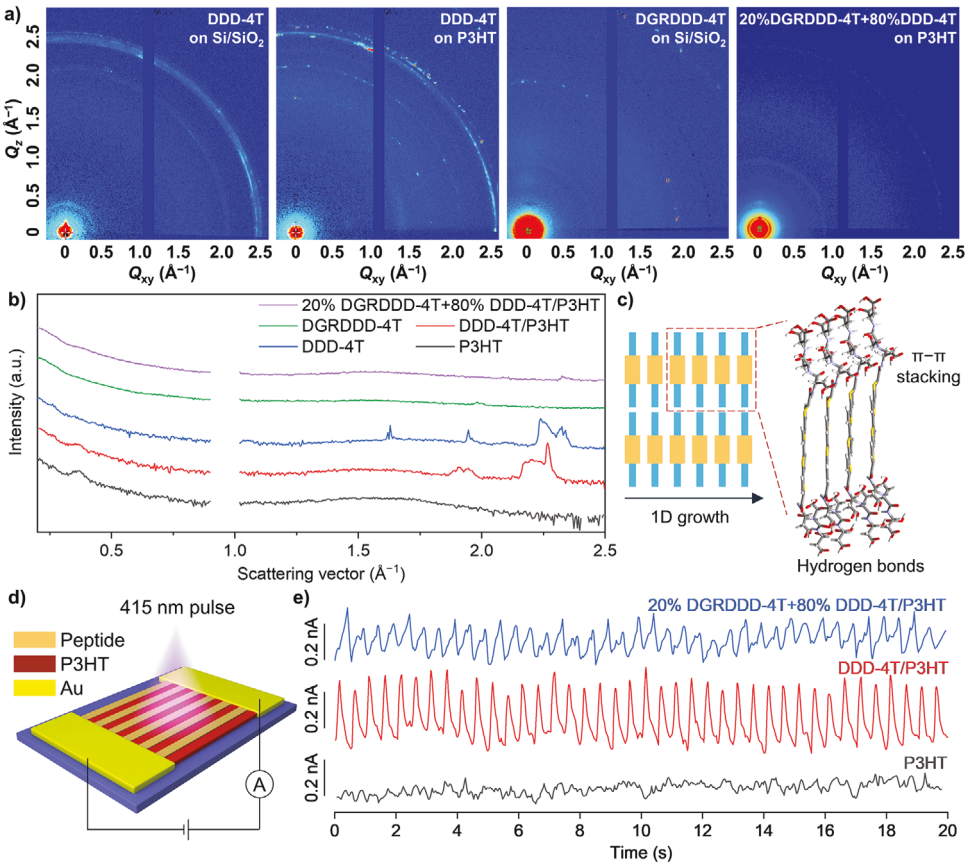

Figure 4. Molecular ordering, charge transport, and photocurrent generation of the assembled nanostructures. a) 2D GIWAXS patterns of DDD-4T, DGRDDD-4T, and their assemblies on P3HT. b) 1D GIWAXS profiles of DDD-4T, DGRDDD-4T, and their assemblies on P3HT. c) Schematic diagram of the molecular packing on substrates. d) Schematic diagram of the device structure and photocurrent measurement. e) Photocurrent generation of the peptide/P3HT substrates under illumination of 415 nm LED light source (16 mW cm^{-2}, 2 Hz).

nanoimprinted P3HT have pattern features here are smaller than those used in the previous lithography-based approaches for patterning in vitro and the micrometer-scale features in native microenvironments. Despite these considerations and noncompliance of NRVMs on bare and FN-coated P3HT, NRVMs demonstrated enhanced alignment on the P3HT substrate with 1D assemblies of DDD-4T or blend of DGRDDD-4T and DDD-4T. To quantify this observation, we fitted the cell orientation angle distribution using the Gaussian peak model and estimated the full width at half maximum (FWHM) with 100 cells from 3 different sample images. For these measurements and subsequent image quantification, we clarify that each biological replicate represents a select region of interest per substrate. The values of FWHM of the cell orientation angle distribution are 115°, 110°, and 122° for glass and P3HT with or without fibronectin (FN), respectively (Figure S15 (Supporting Information); and Figure 5b). This FWHM decreased to 23° with DDD-4T 1D assemblies as the nanotopographical cues on P3HT substrates. For the blend of DGRDDD-4T and DDD-4T, FWHM varied from 96°, 108°, 31°, and 56° with increasing DGRDDD-4T% from 5%, 10%, 20%, to 50%, respectively (Figure S15, Supporting Information). The addition of RGD-containing blend assemblies (Figure 2; and Figure S12, Supporting Information) was expected to improve cell adhesion, yet as shown in GIWAXS data in Figure 4a,b, we note that the degree of molecular ordering of the 20 mol% blend is lower than the DDD-4T assemblies alone. By further characterizing the impact of surface cues here to subcellular organization, we want to assess whether molecular order or presence of adhesive epitopes have a greater impact on cellular features.

In natural cardiac tissues, cytoskeletal actin filament (F-actin) and sarcomeric α-actinin are highly aligned to maximize contraction force.[75,76] We measured the organization of these subcellular features related to cardiac tissue alignment by quantifying the immunofluorescence images of NRVMs seeded under different conditions. Epifluorescence microscopy images (Figure 5c) show the elongated F-actin and cell alignment on peptide-modified substrates where the cardiomyocytes were randomly oriented on P3HT substrates with or without fibronectin, consistent with those shown from the brightfield data. Higher resolution confocal microscopy images of the immunostained cells on peptide-modified substrates clearly demonstrate the alignment of F-actin and sarcomeric α-actinin (Figure 5d; and Figures S16 and S17, Supporting Information). Subsequently, we calculated the OOP values that represent the F-actin and sarcomeric α-actinin orientation of NRVMs under varying surface conditions to further quantify the influence of surface characteristics on cardiomyocyte alignment.[77,78] The estimated OOP values of F-actin are 0.13 ± 0.03, 0.16 ± 0.03, 0.11 ± 0.02, 0.57 ± 0.03, and 0.33 ±

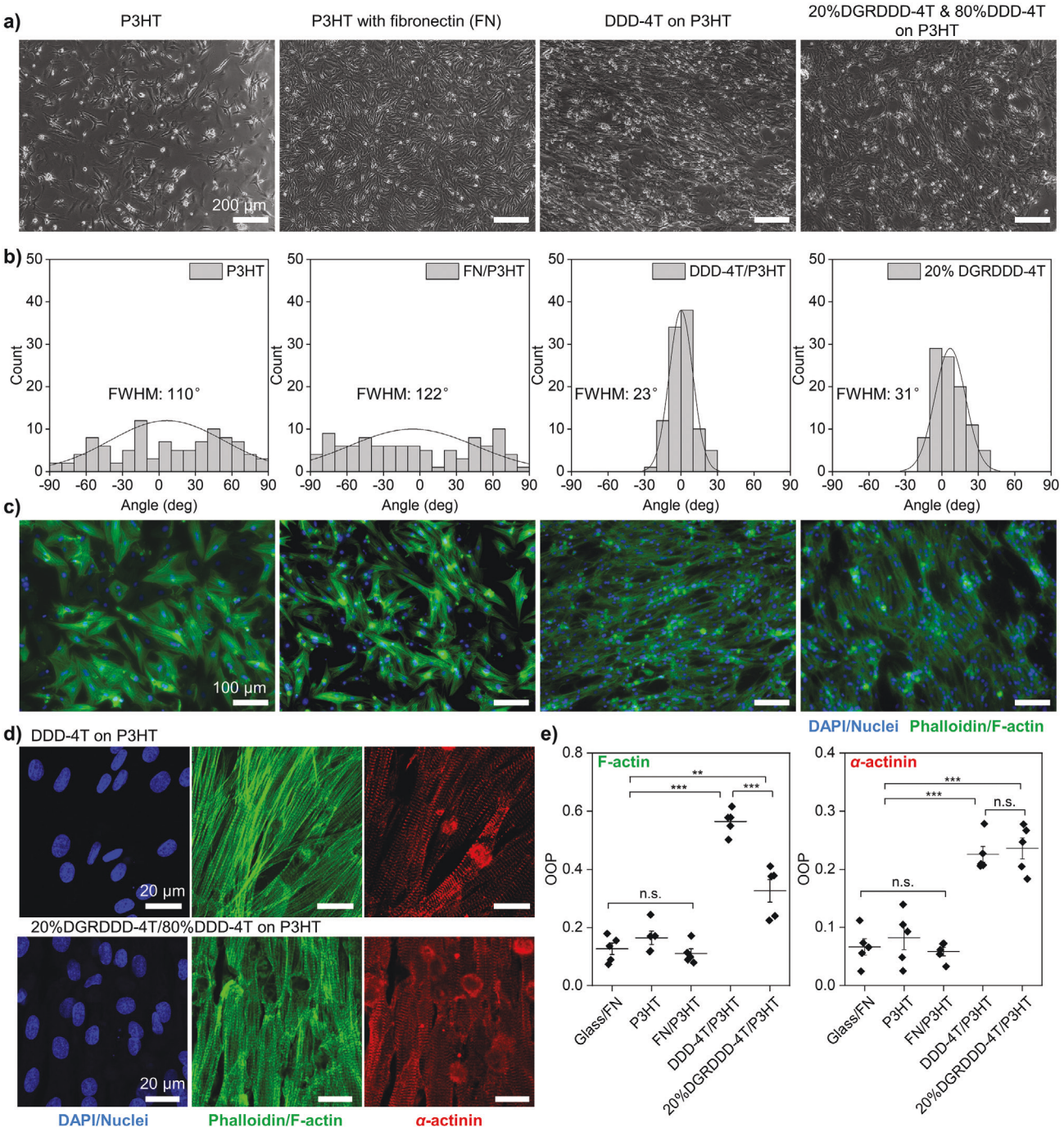

Figure 5. Cellular orientation induced by bare or biomolecule-coupled P3HT substrates. All P3HT substrates were nanoimprinted and patterned. a) Brightfield images. b) Cell angle distributions from the brightfield images. The full width at half maximum (FWHM) is provided to quantitively estimate the cell alignment. 100 cells from 3 different sample images were counted for angle distribution analysis. c) Fluorescence microscope images of stained cells on different substrates. d) Confocal fluorescence microscope images of stained cells on P3HT substrates with DDD-4T assemblies and DGRDDD-4T/DDD-4T blend. e) OOP analysis of F-actin and sarcomeric α-actinin. Data are presented as average values with standard error of the mean, $N = 5$. Statistical analysis was performed using a two-tailed Student's t-test: **: $p < 0.01$; ***: $p < 0.001$; n.s.: not significant, $p > 0.05$.

0.05 (average values ± s.e.m) for the cells on FN-coated glass, P3HT, FN-coated P3HT, DDD-4T on P3HT, and peptide blend on P3HT, respectively. On the other hand, the respective OOP values of sarcomeric α-actinin are 0.07 ± 0.02, 0.08 ± 0.03, 0.06 ± 0.01, 0.23 ± 0.02, and 0.24 ± 0.03 (average values ± s.e.m). Hence, the OOP values of both F-actin and sarcomeric α-actinin significantly increased in the aligned cardiomyocytes on peptide-modified substrates compared to the bare glass or P3HT with or without fibronectin (Figure 5e). Comparing the two conditions with peptide assemblies, there was no significant

difference measured for the sarcomeric OOP between DDD-4T and 20% DGRDDD-4T blend. However, a significant difference was detected for the cytoskeletal OOP between the two conditions, with the surfaces with DDD-4T that have a higher molecular assembly order leading to a higher F-actin OOP value despite the other condition bearing adhesive RGD units. These results demonstrate that the cardiomyocytes differentially responded to the distinct topological cues (with and without -RGD; varying degrees of molecular ordering) provided by 1D peptide assembly on the substrate with ordered nanostructures. This is an important observation, as this is an indication that cardiomyocytes could perceive such differences in local molecular order. Here, we focus on the structural impact of these findings on topological cues via peptide nanostructures, which could inspire future studies on synergistically evaluating the influence of topological and electrical cues across multiple biological length scales. As a reference, other different fabrication approaches have been demonstrated to induce cardiomyocyte alignment, such as microfiber gels, microcontact-printed and nanopatterned surfaces.[11,12,79–85] Most of previous reports used nonconductive polymers with sizes ranging from 50–250 nm to 30–40 μm, differing from our work that shows self-assembled peptides with controlled nanostructures and optoelectronic properties. At this time, while the cardiac biointerface we developed does not have the smallest pattern dimensions reported and more needs to be learned on the impact of different variations of peptide sequences on the surface-guided molecular assembly, we have demonstrated a pioneering example of a cardiac tissue patterning surface template capable of photocurrent-generation. In summary, by quantifying cardiomyocyte anisotropy on different substrates, we revealed some key insights on the sensitivity of cardiomyocytes to comply with submicrometer substrate features, along with presenting a surface-templating platform presented here that can generate ordered 1D assemblies of optoelectronically active peptides toward successfully inducing cardiomyocyte alignment.

3. Conclusion

In this study, we present a nanotemplating approach to influence the order of biomolecular assemblies on polymeric substrates and ultimately, to impact cardiac tissue alignment depending on the nature of biomolecular assemblies at the surface. Our results show that the polyalkylthiophene (P3HT) substrates with nanoimprinted channels can direct the 1D self-assembly of charged peptide-4T (DDD-4T) units due to favorable interactions between the assemblies and the P3HT surface. The formation of high-aspect-ratio 1D structures under mild, close to neutral conditions, was only observed when the peptide-4T solution was deposited on the nanopatterned P3HT, but not when it was on a hydrophilic nanopatterned PDMS substrate or other nonpatterned substrates. The morphological evolution of peptide-4T assembly toward structures with ordered molecular packing was monitored via AFM while the nature of molecular ordering was confirmed using GIWAXS studies. The resulting peptide-4T-P3HT material also demonstrates significantly higher photocurrents as compared to the pristine P3HT surfaces. Interestingly, when cardiomyocytes were seeded on patterned P3HT as a bare surface, coated with an ECM protein, and as a template for DDD-4T and a blend of DDD-4T with its bioadhesive epitope-bearing analog (DGRDDD-4T), only those with self-assembled peptides aligned atop the nanotopographic P3HT led to cytoskeletal and sarcomeric anisotropy that is significantly higher than the isotropic control. Despite the dimensions being smaller than the micropatterns previously reported in the literature to be effective for inducing anisotropy for cardiac tissues (≈20 μm width for grooves), this work shows that cardiomyocytes are capable of perceiving smaller dimensions of topographical cues and can be sensitive to the molecular packing order of the biomolecules interfaced with them. The latter finding is particularly highlighted by the difference between the cytoskeletal OOP between the surfaces with DDD-4T and DDD/DGRDDD-4T blend, where even though the blend carries a bioadhesive RGD epitope, the surface with DDD-4T that has higher molecular order still induced a higher cytoskeletal OOP for the cardiomyocytes. Overall, the self-assembly templating approach of π-conjugated peptides guided by patterned polymeric substrates presented here provides a promising approach for translating conductive supramolecular biomaterials with order toward optoelectronic device applications. Through this platform, we have also unveiled important insights on the sensitivity of cardiac tissues to the molecular composition and order of the biomolecules that comprise its microenvironment. Finally, we envision that photocurrent-generating biointerfaces, such as the one presented here, will aid in advancing the mechanisms available for modulating the in situ electromechanical function of non-genetically modified cardiac tissues as needed for several cardiac regenerative medicine applications.

4. Experimental Section

Experimental details can be founded in the Supporting Information, including material information, peptide synthesis, molecular simulations, polymer film fabrication and peptide assembly, spectral and morphological characterizations, device fabrication and photocurrent measurement, cell culture and imaging.

Statistical Analysis: All plotted curves were processed using OriginLab software and all values were presented by mean ± s.e.m. Cell images were processed using ImageJ. OOP of aligned cells were calculated using the codes from Grosberg et al.,[77,78] which can be downloaded at GitHub website: https://github.com/Cardiovascular-Modeling-Laboratory/zlineDetection. Two-tailed Student's *t*-test was used to assess the statistical significance of differences in reported OOP values.

Supporting Information

Supporting Information is available from the Wiley Online Library or from the author.

Acknowledgements

This work was supported by the National Heart, Lung, And Blood Institute (NHLBI) of the National Institutes of Health (NIH) under Award Nos. R56HL164348 andR01HL164348. The authors also acknowledge support from the University of California, Irvine (UCI), as well as partial support from the seed grant from National Science Foundation Materials Research Science and Engineering Center at UC Irvine (Center for Complex and Active Materials; DMR-2011967). The authors acknowledge the use of facilities and instrumentation at the UC Irvine Materials Research Institute (IMRI), which is also supported in part by the National Science Foundation Materials Research Science and Engineering Center: Center for Complex

and Active Materials (DMR-2011967). The authors acknowledge the Research Cyberinfrastructure Center (RCIC) at UCI for supporting the computational work. The authors acknowledged the NIH S10 equipment grant (1S10OD025064) that provided support for the confocal microscope used in this study. The authors thank Dr. Dmitry Fishman at UCI for the access to equipment in the Laser SpectroscopyLaboratories, as well as Prof. Camilo Velez Cuervo for the access to a Keithley 4200 SCS semiconductor parameter analyzer.

Conflict of interest

The authors declare no conflict of interest.

Author Contributions

The authors listed above have all substantially contributed to this work and have approved the final version of the manuscript.

Data Availability Statement

The data that support the findings of this study are available from the corresponding author upon reasonable request.

Keywords

cardiac tissue engineering, optoelectronics, peptides, self-assembly, tissue anisotropy

Received: November 15, 2023
Revised: January 19, 2024
Published online:

[1] E. C. Miner, W. L. Miller, *Mayo Clin. Proc.* **2006**, *81*, 71.
[2] C. Frantz, K. M. Stewart, V. M. Weaver, *J. Cell Sci.* **2010**, *123*, 4195.
[3] B. C. Berk, K. Fujiwara, S. Lehoux, *J. Clin. Invest.* **2007**, *117*, 568.
[4] E. Bassat, Y. E. Mutlak, A. Genzelinakh, I. Y. Shadrin, K. Baruch Umansky, O. Yifa, D. Kain, D. Rajchman, J. Leach, D. Riabov Bassat, Y. Udi, R. Sarig, I. Sagi, J. F. Martin, N. Bursac, S. Cohen, E. Tzahor, *Nature* **2017**, *547*, 179.
[5] S. Hinds, W. Bian, R. G. Dennis, N. Bursac, *Biomaterials* **2011**, *32*, 3575.
[6] K. Ronaldson-Bouchard, S. P. Ma, K. Yeager, T. Chen, L. Song, D. Sirabella, K. Morikawa, D. Teles, M. Yazawa, G. Vunjak-Novakovic, *Nature* **2018**, *556*, 239.
[7] Y. Guo, W. T. Pu, *Circ. Res.* **2020**, *126*, 1086.
[8] S. Cho, D. E. Discher, K. W. Leong, G. Vunjak-Novakovic, J. C. Wu, *Nat. Methods* **2022**, *19*, 1064.
[9] C. Williams, K. Sullivan, L. D. Black, *Adv. Healthcare Mater.* **2015**, *4*, 1545.
[10] C. Williams, K. P. Quinn, I. Georgakoudi, L. D. Black, *Acta Biomater.* **2014**, *10*, 194.
[11] C.-W. Hsiao, M.-Y. Bai, Y. Chang, M.-F. Chung, T.-Y. Lee, C.-T. Wu, B. Maiti, Z.-X. Liao, R.-K. Li, H.-W. Sung, *Biomaterials* **2013**, *34*, 1063.
[12] S. Choi, K. Y. Lee, S. L. Kim, L. A. MacQueen, H. Chang, J. F. Zimmerman, Q. Jin, M. M. Peters, H. A. M. Ardoña, X. Liu, A. Heiler, R. Gabardi, C. Richardson, W. T. Pu, A. R. Bausch, K. K. Parker, *Nat. Mater.* **2023**, *22*, 1039.
[13] D.-H. Kim, P. K. Wong, J. Park, A. Levchenko, Y. Sun, *Annu. Rev. Biomed. Eng.* **2009**, *11*, 203.
[14] S. Zhang, *Nat. Biotechnol.* **2003**, *21*, 1171.
[15] N. J. Sinha, M. G. Langenstein, D. J. Pochan, C. J. Kloxin, J. G. Saven, *Chem. Rev.* **2021**, *121*, 13915.
[16] Z.-F. Yao, E. Lundqvist, Y. Kuang, H. A. M. Ardoña, *Adv. Sci.* **2023**, *10*, 2205381.
[17] F.-M. Chen, X. Liu, *Prog. Polym. Sci.* **2016**, *53*, 86.
[18] D. M. Bers, *Nature* **2002**, *415*, 198.
[19] H. A. Feridooni, K. M. Dibb, S. E. Howlett, *J. Mol. Cell. Cardiol.* **2015**, *83*, 62.
[20] E. Karbassi, A. Fenix, S. Marchiano, N. Muraoka, K. Nakamura, X. Yang, C. E. Murry, *Nat. Rev. Cardiol.* **2020**, *17*, 341.
[21] Y. Li, L. Wei, L. Lan, Y. Gao, Q. Zhang, H. Dawit, J. Mao, L. Guo, L. Shen, L. Wang, *Acta Biomater.* **2022**, *139*, 157.
[22] A. Burnstine-Townley, Y. Eshel, N. Amdursky, *Adv. Funct. Mater.* **2020**, *30*, 1901369.
[23] H. He, H. Li, A. Pu, W. Li, K. Ban, L. Xu, *Nat. Commun.* **2023**, *14*, 759.
[24] N. Tandon, C. Cannizzaro, P. H. G. Chao, R. Maidhof, A. Marsano, H. T. H. Au, M. Radisic, G. Vunjak-Novakovic, *Nat. Protoc.* **2009**, *4*, 155.
[25] M. Ghovvati, M. Kharaziha, R. Ardehali, N. Annabi, *Adv. Healthcare Mater.* **2022**, *11*, 2200055.
[26] L. Scott, K. Elídóttir, K. Jeevaratnam, I. Jurewicz, R. Lewis, *Ann. N. Y. Acad. Sci.* **2022**, *1515*, 105.
[27] R. Parameswaran, K. Koehler, M. Y. Rotenberg, M. J. Burke, J. Kim, K.-Y. Jeong, B. Hissa, M. D. Paul, K. Moreno, N. Sarma, T. Hayes, E. Sudzilovsky, H.-G. Park, B. Tian, *Proc. Natl. Acad. Sci. USA* **2019**, *116*, 413.
[28] V. Vurro, B. Federici, C. Ronchi, C. Florindi, V. Sesti, S. Crasto, C. Maniezzi, C. Galli, M. R. Antognazza, C. Bertarelli, E. Di Pasquale, G. Lanzani, F. Lodola, *iScience* **2023**, *26*, 106121.
[29] V. Vurro, K. Shani, H. A. M. Ardoña, J. F. Zimmerman, V. Sesti, K. Y. Lee, Q. Jin, C. Bertarelli, K. K. Parker, G. Lanzani, *APL Bioeng.* **2023**, *7*, 026108.
[30] B. D. Wall, S. R. Diegelmann, S. Zhang, T. J. Dawidczyk, W. L. Wilson, H. E. Katz, H.-Q. Mao, J. D. Tovar, *Adv. Mater.* **2011**, *23*, 5009.
[31] J. S. Lee, I. Yoon, J. Kim, H. Ihee, B. Kim, C. B. Park, *Angew. Chem., Int. Ed.* **2011**, *50*, 1164.
[32] H. A. M. Ardoña, E. R. Draper, F. Citossi, M. Wallace, L. C. Serpell, D. J. Adams, J. D. Tovar, *J. Am. Chem. Soc.* **2017**, *139*, 8685.
[33] H. A. M. Ardoña, J. D. Tovar, *Bioconjug. Chem.* **2015**, *26*, 2290.
[34] Q.-Y. Li, Z.-F. Yao, J.-Y. Wang, J. Pei, *Rep Prog. Phys.* **2021**, *84*, 076601.
[35] X. Yan, P. Zhu, J. Li, *Chem. Soc. Rev.* **2010**, *39*, 1877.
[36] A. M. Sanders, T. J. Magnanelli, A. E. Bragg, J. D. Tovar, *J. Am. Chem. Soc.* **2016**, *138*, 3362.
[37] Q. Zou, K. Liu, M. Abbas, X. Yan, *Adv. Mater.* **2016**, *28*, 1031.
[38] O. Ostroverkhova, *Chem. Rev.* **2016**, *116*, 13279.
[39] H. Bronstein, C. B. Nielsen, B. C. Schroeder, I. McCulloch, *Nat. Rev. Chem.* **2020**, *4*, 66.
[40] Y. Bin Lee, S. Kim, E. M. Kim, H. Byun, H. Chang, J. Park, Y. S. Choi, H. Shin, *Acta Biomater.* **2017**, *61*, 75.
[41] D.-H. Kim, E. A. Lipke, P. Kim, R. Cheong, S. Thompson, M. Delannoy, K.-Y. Suh, L. Tung, A. Levchenko, *Proc. Natl. Acad. Sci. USA* **2010**, *107*, 565.
[42] K. Wang, K. Man, J. Liu, B. Meckes, Y. Yang, *ACS Nano* **2023**, *17*, 2124.
[43] K. Tao, P. Makam, R. Aizen, E. Gazit, *Science* **2017**, *358*, eaam9756.
[44] S. S. Panda, H. E. Katz, J. D. Tovar, *Chem. Soc. Rev.* **2018**, *47*, 3640.
[45] S. Park, Y. J. Kang, S. Majd, *Adv. Mater.* **2015**, *27*, 7583.
[46] P. Singh, C. Carraher, J. E. Schwarzbauer, *Annu. Rev. Cell Dev. Biol.* **2010**, *26*, 397.
[47] I. J. Domian, M. Chiravuri, P. van der Meer, A. W. Feinberg, X. Shi, Y. Shao, S. M. Wu, K. K. Parker, K. R. Chien, *Science* **2009**, *326*, 426.
[48] H. A. M. Ardoña, K. Besar, M. Togninalli, H. E. Katz, J. D. Tovar, *J. Mater. Chem. C* **2015**, *3*, 6505.
[49] Z.-F. Yao, Y. Kuang, P. Kohl, Y. Li, H. A. M. Ardoña, *ChemSystemsChem* **2023**, *5*, 202300003.

[50] E. K. Schillinger, E. Mena-Osteritz, J. Hentschel, H. G. Börner, P. Bäuerle, *Adv. Mater.* **2009**, *21*, 1562.
[51] O. P. Dimitriev, *Chem. Rev.* **2022**, *122*, 8487.
[52] S. Grimme, C. Bannwarth, P. Shushkov, *J. Chem. Theory Comput.* **2017**, *13*, 1989.
[53] G. A. Kaminski, R. A. Friesner, J. Tirado-Rives, W. L. Jorgensen, *J. Phys. Chem. B* **2001**, *105*, 6474.
[54] R. Marty, R. Nigon, D. Leite, H. Frauenrath, *J. Am. Chem. Soc.* **2014**, *136*, 3919.
[55] L. Tan, Y. P. Kong, L.-R. Bao, X. D. Huang, L. J. Guo, S. W. Pang, A. F. Yee, *J. Vac. Sci. Technol. B: Microelectron. Nanom. Struct.* **2003**, *21*, 2742.
[56] Y. Yang, K. Mielczarek, M. Aryal, A. Zakhidov, W. Hu, *ACS Nano* **2012**, *6*, 2877.
[57] G. Ding, Y. Wu, Y. Weng, W. Zhang, Z. Hu, *Macromolecules* **2013**, *46*, 8638.
[58] Z. Zheng, K.-H. Yim, M. S. M. Saifullah, M. E. Welland, R. H. Friend, J.-S. Kim, W. T. S. Huck, *Nano Lett.* **2007**, *7*, 987.
[59] M. Aryal, K. Trivedi, W. Walter Hu, *ACS Nano* **2009**, *3*, 3085.
[60] I. Batalov, Q. Jallerat, S. Kim, J. Bliley, A. W. Feinberg, *Sci. Rep.* **2021**, *11*, 11502.
[61] H. Chang, Q. Liu, J. F. Zimmerman, K. Y. Lee, Q. Jin, M. M. Peters, M. Rosnach, S. Choi, S. L. Kim, H. A. M. Ardoña, L. A. MacQueen, C. O. Chantre, S. E. Motta, E. M. Cordoves, K. K. Parker, *Science* **2022**, *377*, 180.
[62] A. K. Capulli, L. A. MacQueen, S. P. Sheehy, K. K. Parker, *Adv. Drug Delivery Rev.* **2016**, *96*, 83.
[63] Z.-F. Yao, J.-Y. Wang, J. Pei, *Cryst. Growth Des.* **2018**, *18*, 7.
[64] E. R. Draper, J. J. Walsh, T. O. McDonald, M. A. Zwijnenburg, P. J. Cameron, A. J. Cowan, D. J. Adams, *J. Mater. Chem. C* **2014**, *2*, 5570.
[65] E. R. Draper, J. R. Lee, M. Wallace, F. Jäckel, A. J. Cowan, D. J. Adams, *Chem. Sci.* **2016**, *7*, 6499.
[66] E. R. Draper, B. J. Greeves, M. Barrow, R. Schweins, M. A. Zwijnenburg, D. J. Adams, *Chem* **2017**, *2*, 716.
[67] Y. Xiang, H. Mao, S. Tong, C. Liu, R. Yan, L. Zhao, L. Zhu, C. Bao, *ACS Nano* **2023**, *17*, 5536.
[68] Y.-S. Hsiao, C.-C. Lin, H.-J. Hsieh, S.-M. Tsai, C.-W. Kuo, C.-W. Chu, P. Chen, *Lab Chip* **2011**, *11*, 3674.
[69] G. Zhang, W. Li, M. Yu, H. Huang, Y. Wang, Z. Han, K. Shi, L. Ma, Z. Yu, X. Zhu, Z. Peng, Y. Xu, X. Li, S. Hu, J. He, D. Li, Y. Xi, H. Lan, L. Xu, M. Tang, M. Xiao, *Adv. Sci.* **2023**, *10*, 2206264.
[70] A. House, I. Atalla, E. J. Lee, M. Guvendiren, *Adv. Nanobiomed. Res.* **2021**, *1*, 2000022.
[71] B. K. K. Teo, S. T. Wong, C. K. Lim, T. Y. S. Kung, C. H. Yap, Y. Ramagopal, L. H. Romer, E. K. F. Yim, *ACS Nano* **2013**, *7*, 4785.
[72] A. W. Feinberg, P. W. Alford, H. Jin, C. M. Ripplinger, A. A. Werdich, S. P. Sheehy, A. Grosberg, K. K. Parker, *Biomaterials* **2012**, *33*, 5732.
[73] T. Takada, D. Sasaki, K. Matsuura, K. Miura, S. Sakamoto, H. Goto, T. Ohya, T. Iida, J. Homma, T. Shimizu, N. Hagiwara, *Biomaterials* **2022**, *281*, 121351.
[74] Y. Gong, Z. Chen, L. Yang, X. Ai, B. Yan, H. Wang, L. Qiu, Y. Tan, N. Witman, W. Wang, Y. Zhao, W. Fu, *ACS Nano* **2020**, *14*, 8232.
[75] M. Bray, S. P. Sheehy, K. K. Parker, *Cell Motil.* **2008**, *65*, 641.
[76] A. Grosberg, P.-L. Kuo, C.-L. Guo, N. A. Geisse, M.-A. Bray, W. J. Adams, S. P. Sheehy, K. K. Parker, *PLoS Comput. Biol.* **2011**, *7*, 1001088.
[77] T. A. Morris, J. Naik, K. S. Fibben, X. Kong, T. Kiyono, K. Yokomori, A. Grosberg, *PLoS Comput. Biol.* **2020**, *16*, 1007676.
[78] F. S. Pasqualini, S. P. Sheehy, A. Agarwal, Y. Aratyn-Schaus, K. K. Parker, *Stem Cell Rep.* **2015**, *4*, 340.
[79] A. W. Feinberg, A. Feigel, S. S. Shevkoplyas, S. Sheehy, G. M. Whitesides, K. K. Parker, *Science* **2007**, *317*, 1366.
[80] C.-Y. Su, A. Burchett, M. Dunworth, J. S. Choi, A. J. Ewald, E. H. Ahn, D.-H. Kim, *Biomaterials* **2021**, *275*, 120922.
[81] J. H. Tsui, K. Janebodin, N. Ieronimakis, D. M. P. Yama, H. S. Yang, R. Chavanachat, A. L. Hays, H. Lee, M. Reyes, D.-H. Kim, *ACS Nano* **2017**, *11*, 11954.
[82] H. S. Yang, B. Lee, J. H. Tsui, J. Macadangdang, S.-Y. Jang, S. G. Im, D.-H. Kim, *Adv. Healthcare Mater.* **2016**, *5*, 137.
[83] A. Jiao, N. E. Trosper, H. S. Yang, J. Kim, J. H. Tsui, S. D. Frankel, C. E. Murry, D.-H. Kim, *ACS Nano* **2014**, *8*, 4430.
[84] W. Bian, B. Liau, N. Badie, N. Bursac, *Nat. Protoc.* **2009**, *4*, 1522.
[85] W. Bian, N. Badie, H. D. Himel, N. Bursac, *Biomaterials* **2014**, *35*, 3819.